J. Fluid Mech. (2021), *vol*. 917, R1, doi:10.1017/jfm.2021.333

Effects of power-law entrainment on bubble fragmentation cascades

Declan B. Gaylo[1], **Kelli Hendrickson**[1] **and Dick K.P. Yue**[1],†

[1]Department of Mechanical Engineering, Massachusetts Institute of Technology, Cambridge, MA 02139, USA

(Received 23 February 2021; revised 23 March 2021; accepted 3 April 2021)

We consider the evolution of the bulk bubble-size distribution $N(a, t)$ of large bubbles (Weber number $We \gg 1$) under free-surface entrainment described generally by an entrainment size distribution $I(a)$ with power-law slope γ and large-radius cutoff a_{max}. Our main focus is the interaction between turbulence-driven fragmentation and free-surface entrainment, and, for simplicity, we ignore other mechanisms such as degassing, coalescence and dissolution. Of special interest are the equilibrium bulk distribution $N_{eq}(a)$, with local power-law slope $\tilde{\beta}_{eq}(a)$, and the time scale τ_c to reach this equilibrium after initiation of entrainment. For bubble radii $a \ll a_{max}$, we find two regimes for the dependence of $N_{eq}(a)$ on the entrainment distribution. There is a weak injection regime for $\gamma \geq -4$, where $\tilde{\beta}_{eq}(a) = -10/3$ independent of the entrainment distribution; and a strong injection regime for $\gamma < -4$, where the power-law slope depends on γ and is given by $\tilde{\beta}_{eq}(a) = \gamma + 2/3$. The weak regime provides a general explanation for the commonly observed $-10/3$ power law originally proposed by Garrett *et al.* (*J. Phys. Oceanogr.*, vol. 30 (9), 2000, pp. 2163–2171), and suggests that different weak entrainment mechanisms can all lead to this result. For $a \sim a_{max}$, we find that $N_{eq}(a)$ exhibits a steepening deviation from a power law due to fragmentation and entrainment, similar to what has been observed, but here absent other mechanisms such as degassing. The evolution of $N(a, t)$ to $N_{eq}(a)$ is characterised by the critical time $\tau_c \propto C_f \varepsilon^{-1/3} {a_{max}}^{2/3}$, where ε is the turbulence dissipation rate and C_f is a new constant that quantifies the dependence on the daughter size distribution in a fragmentation event. For typical breaking waves, τ_c can be quite small, limiting the time $t \lesssim \tau_c$ when direct measurement of $N(a, t)$ might provide information about the underlying entrainment size distribution.

Key words: bubble dynamics, breakup/coalescence

† Email address for correspondence: yue@mit.edu

1. Introduction

Air-entraining bubbly flows are relevant to a variety of natural and engineering applications, including liquid metal fast breeder reactors (Patwardhan *et al.* 2012), sea-surface gas exchange due to breaking waves (Thorpe 1982), water quality in lakes and rivers, and the wake around ships (Castro, Li & Carrica 2016). An important characteristic of these flows is the size of bubbles within the fluid, as described by the bubble-size distribution. This distribution is the result of fragmentation, coalescence, dissolution, entrainment and degassing. There has been significant study of the first three mechanisms, especially fragmentation (Liao & Lucas 2009; Martínez-Bazán *et al.* 2010; Qi, Mohammad Masuk & Ni 2020). In this work, we focus directly on the relationship between turbulent fragmentation and entrainment, the original source of the bubbles, ignoring coalescence, dissolution and degassing. Thus the present results would directly apply to flows with small void fractions (where coalescence is less important), and for relatively short times (before dissolution and degassing play significant roles). For the more general problem, our results provide useful insight into the interaction dynamics between entrainment and fragmentation even in the presence of the other mechanisms.

Direct measurement of entrainment is difficult due to proximity to a necessarily complex free surface. Thus characteristics of entrainment such as the entrainment size distribution $I(a)$ are often inferred from the bulk bubble-size distribution $N(a, t)$ (Yu *et al.* 2019). (Here the effective bubble radius a is typically defined in terms of the bubble volume V by $a = (3V/4\pi)^{1/3}$.) However, the link between $I(a)$ and the resulting $N(a, t)$ is still not well understood. Recent work (Yu, Hendrickson & Yue 2020) suggests that entrainment follows a power-law size distribution $I(a) \propto a^{\gamma}$, contrary to the current simplifying assumption, $I(a) \propto \delta(a - a_{max})$ (Garrett, Li & Farmer 2000), where δ is the Dirac delta function. The objective of the present work is to elucidate the connection between an entrainment process following a general power-law distribution and the resultant bubble-size distribution. Of particular interest are the equilibrium bulk bubble-size distribution $N_{eq}(a)$ and the time scale τ_c for this equilibrium to be reached after the initiation of entrainment.

A well-established scale in fragmentation is the Hinze scale a_H (Hinze 1955), which delineates the length scale where surface tension prevents fragmentation by local turbulent velocity fluctuations. For isotropic homogeneous turbulent (IHT) flows, velocity fluctuations within the Kolmogorov inertial sub-range are described by an energy cascade, and the turbulent Weber number is given by $We = \rho 2\varepsilon^{2/3}(2a)^{5/3}\sigma^{-1}$, where ρ is the density of the surrounding fluid, σ is the surface tension coefficient and ε is the turbulent dissipation rate. The Hinze scale occurs at the critical turbulent Weber number $We_c \approx 4.7$ (Lewis & Davidson 1982; Martínez-Bazán, Montañés & Lasheras 1999*a*). For $a \gg a_H$ ($We \gg We_c$), velocity fluctuations dominate and, assuming IHT, a mechanistic argument can be used to determine the expected life of a bubble from creation to fragmentation, the reciprocal of which is the expected breakup frequency (Martínez-Bazán *et al.* 1999*a*, 2010; Garrett *et al.* 2000):

$$\Omega(a) = C_{\Omega}\varepsilon^{1/3}a^{-2/3}. \tag{1.1}$$

Experiments suggest $C_{\Omega} \approx 0.42$ (Martínez-Bazán *et al.* 1999*a*; Rodríguez-Rodríguez, Gordillo & Martínez-Bazán 2006).

For bubbles with $a > a_H$, Garrett *et al.* (2000) developed a fragmentation (only) cascade model by assuming all bubbles are injected at a single radius a_{max}, $I(a) \propto \delta(a - a_{max})$, and fragment into m identical daughter bubbles. Using (1.1), the resulting equilibrium bubble-size distribution $N_{eq}(a)$ is

$$N_{eq}(a) \propto Q\varepsilon^{-1/3}a^{\beta}, \quad \beta = -10/3, \tag{1.2}$$

where Q is the steady volumetric flow rate of air being injected. Bulk bubble-size distributions reasonably described by a power-law slope around $\beta \approx -10/3$ for $a > a_H$ are observed during entrainment in a variety of air-entraining bubbly flows (Deane & Stokes 2002; Blenkinsopp & Chaplin 2010; Deane, Stokes & Callaghan 2016; Deike, Melville & Popinet 2016; Wang, Yang & Stern 2016; Hendrickson, Yu & Yue 2020; Yu *et al.* 2020; Chan *et al.* 2021). Droplet equilibrium distributions following a $-10/3$ power law have also been observed due to fragmentation and coalescence (without injection) at high void fractions (Skartlien, Sollum & Schumann 2013; Mukherjee *et al.* 2019); however, it is not clear how the effect of coalescence is related to the entrainment we study here.

Recent work by Yu *et al.* (2020) provides an alternative explanation for $\beta = -10/3$. While studying entraining free-surface turbulence in direct numerical simulations, they observed bubbles being entrained over a broad range of sizes. Comparing the interfacial and gravitational potential energy of newly formed bubbles to the kinetic energy available from nearby turbulence at similar scales, they provide an argument that this entrainment follows a power-law distribution of slope $\gamma = -10/3$ for large (Bond number $We/Fr^2 \gg 1$) bubbles. This would cause a bulk bubble-size distribution with power-law slope $\beta \approx \gamma$ during some initial time before the effects of fragmentation and other mechanisms come into play.

Considering the fragmentation cascade used by Garrett *et al.* (2000), Deike *et al.* (2016) proposed a critical time

$$\tau_c \propto c_{q,m} \varepsilon^{-1/3} {a_{max}}^{2/3} \tag{1.3}$$

for convergence to the equilibrium described by (1.2), based on the number of identical fragmentation events q to go from a bubble of radius a_{max} to a_H. Recent work by Qi *et al.* (2020) (also assuming $I(a) \propto \delta(a - a_{max})$) suggests τ_c should depend on the daughter bubble-size distribution, and that identical fragmentation only represents a lower bound on τ_c. A power-law entrainment distribution $I(a) \propto a^\gamma$ as suggested by Yu *et al.* (2020) could also lead to an equilibrium, but neither the resulting $N_{eq}(a)$ nor τ_c has been described. By considering the interaction between power-law entrainment and fragmentation, we are able to create a general description of $N_{eq}(a)$ and τ_c, including a quantification of the effects of different daughter bubble-size distributions.

Section 2 develops a population balance model describing realistic steady injection of bubbles following a power law $I(a) \propto a^\gamma$ and fragmentation for $a > a_H$, which allows us to study the interaction between power-law entrainment, such as that proposed by Yu *et al.* (2020), and fragmentation. Section 3 determines the resulting $N_{eq}(a)$ with its local slope $\tilde{\beta}_{eq}(a)$ dependent on γ in two regimes, providing insight into what observations of $\beta \approx -10/3$ tell us about $I(a)$. Section 4 determines the critical time scale τ_c for convergence to $N_{eq}(a)$ under power-law injection, including a quantification of its dependence upon the distribution of daughter bubbles. Simulations show the effect of fragmentation quickly becomes important, even at times $t \ll \tau_c$. Finally, § 5 shows that the interaction between a realistic entrainment distribution and fragmentation (alone) results in steepening of the bubble-size distribution similar to what has been observed in the literature.

2. Describing injection-driven fragmentation cascades

We consider the population density function $n(a, \boldsymbol{x}, t)$ (dimension L^{-4}) where $n(a, \boldsymbol{x}, t)\delta a \delta \boldsymbol{x}$ is the number of bubbles of radius $a < a' < a + \delta a$ in a volume $\delta \boldsymbol{x}$ around a specified location $\boldsymbol{x}$ at time t. A Boltzmann-type population balance model describes the

evolution of n (Williams 1985, chap. 11):

$$\partial n/\partial t + \boldsymbol{\nabla} \cdot (\bar{\boldsymbol{v}} n) = s_d + s_b + s_c, \tag{2.1}$$

where $\bar{\boldsymbol{v}}$ is the mean velocity of bubbles of the given radii, and s_d, s_b and s_c are respectively the movement of air between bubble sizes due to dissolution, fragmentation and coalescence. For locally uniform flows, integrating $n(a, \boldsymbol{x}, t)$ over the domain, we define the bulk bubble-size distribution $N(a, t)$, of dimension L^{-1}. Integrating s_b over the domain yields the bulk fragmentation contribution S_b:

$$S_b(a, t) = -\Omega(a) N(a, t) + \int_a^\infty m(a') f(a; a') \Omega(a') N(a', t)\, \mathrm{d}a', \tag{2.2}$$

where $m(a')$ is the number of daughter bubbles created during the breakup of a parent of radius a' and $f(a; a')$ is the radius-based probability density function (p.d.f.) describing the radius a of daughter bubbles created by that breakup (Liao & Lucas 2009; Martínez-Bazán *et al.* 2010).

For simplicity, we focus on the relationship between entrainment and fragmentation, ignoring coalescence, dissolution and degassing. Thus,

$$\partial N/\partial t(a, t) = S_b(a, t) + I(a) \tag{2.3}$$

defines the population balance model for an injection-driven fragmentation cascade with $I(a)$ the (steady) inflow of bubbles into the domain due to entrainment. Our interest is for $a > a_H$, and, as modelled, $N(a, t)$ depends only on scales larger than a; thus, sub-Hinze-scale mechanisms can be ignored.

2.1. *A simple population balance model (S-PBM) for fragmentation cascades*

An analytic solution to $N(a, t)$ requires a simplified description of S_b. To satisfy volume conservation and the definition of a p.d.f., $f(a'; a)$ must satisfy the following (Martínez-Bazán *et al.* 2010):

$$m(a) \int_0^a (a'/a)^3 f(a'; a)\, \mathrm{d}a' = 1, \quad \int_0^a f(a'; a)\, \mathrm{d}a' = 1. \tag{2.4a,b}$$

For simplicity, we assume a bubble breaks up into m (independent of a) identical bubbles (Garrett *et al.* 2000). Satisfying (2.4*a*,*b*) produces the identical daughter distribution (Valentas, Bilous & Amundson 1966)

$$f(a'; a) = \delta(a' - a m^{-1/3}). \tag{2.5}$$

Equation (2.5) makes analytic evaluation in §§ 2.2 and 3.1 possible. §§ 3.2 and 4 consider more realistic daughter distributions from literature. Combining (2.2) and (2.5), and upon integration with a change of variable for the delta function, we obtain

$$S_b(a, t) = -\Omega(a) N(a, t) + m^{1/3}[m\Omega(m^{1/3} a) N(m^{1/3} a, t)]. \tag{2.6}$$

Using (1.1) and (2.6), we simplify (2.3) and define the simple population balance model (S-PBM) as

$$\partial N^*/\partial t^*(a^*, t^*) = a^{*-2/3}[-N^*(a^*, t^*) + m^{10/9} N^*(m^{1/3} a^*, t^*)] + I^*(a^*), \tag{2.7}$$

where $\cdot^*$ denotes nondimensionalisation using the characteristic bubble radius $L = a_{max}$ and time $T = \Omega(a_{max})^{-1}$.

2.2. *Scale-invariant solutions to S-PBM*

We consider solutions to (2.7) where $N^*(a^*, t^*) = a^{*\beta} g(t^*)$ for all $a \in (0, \infty)$, defining $g(t^*)$ to be only a function of time. Substituting into (2.7) gives

$$\mathrm{d}g/\mathrm{d}t^* = g a^{*-2/3}(-1 + m^{\beta/3+10/9}) + a^{*-\beta} I^*(a^*). \tag{2.8}$$

For $g(t^*)$ to be independent of a^* and injection to be non-trivial, I^* must also be scale-invariant: $I^*(a) = h a^{*\gamma}$ for all $a \in (0, \infty)$, where h is a constant, and the power-law slope is γ. There are only two admissible solutions for the form of N^* we consider. The first is a transient solution in which $\beta = \gamma = -10/3$ and $\mathrm{d}g/\mathrm{d}t^* = h$, resulting in $S_b = 0$. This ($S_b = 0$) is equivalent to the condition imposed by Garrett *et al.* (2000) to represent an equilibrium for their fragmentation cascade. The second solution is a steady-state solution in which $\beta = \gamma + 2/3$ and $\mathrm{d}g/\mathrm{d}t^* = 0$. Both admissible solutions have physical limitations. To describe the commonly observed $\beta = -10/3$, they would suggest $\gamma = -10/3$ or $\gamma = -4$; however, $\gamma \geq -4$ implies an infinite rate of volume injection.

3. Equilibrium solutions for cutoff spectral injection

Based on the mechanistic energy argument by Yu *et al.* (2020) and § 2.2, we assume an entrainment size distribution described by a power law of slope γ. To ensure a finite rate of volume injection, we introduce a cutoff radius a_{max} above which there is no bubble injection. In addition to ensuring finite injected volume if $\gamma \geq -4$, physical limits of a flow will necessarily impose some a_{max}. For example, Yu *et al.* (2020) proposed an a_{max} for entraining free-surface turbulence based on bubble Froude number. The cutoff spectral injection model (SIM) is thus

$$I^* = h(a^*)^\gamma \mathcal{H}(1 - a^*), \tag{3.1}$$

where $\mathcal{H}$ is the Heaviside step function. Note that (3.1) is a generalization of Garrett *et al.* (2000), which corresponds to $\gamma \to \infty$ (all bubbles injected at $a = a_{max}$). In § 4, we show that under SIM, $N(a, t)$ approaches an equilibrium $N_{eq}(a)$ in a time scale given by τ_c.

SIM allows us to define a new global condition for equilibrium: the volume flux of air injected as bubbles larger than a must be equal to the volume flux of air from bubbles larger than a to bubbles smaller than a due to fragmentation; i.e.,

$$\int_{a^*}^{\infty} I^*(r) r^3 \,\mathrm{d}r = \int_{a^*}^{\infty} N^*_{eq}(r) \Omega^*(r) m \int_0^{a^*} r'^3 f^*(r'; r) \,\mathrm{d}r' \,\mathrm{d}r, \tag{3.2}$$

where the integration variables r and r' are dimensionless (scaled by a_{max}).

3.1. *Local power-law slope of the equilibrium bulk bubble-size distribution*

Rather than assuming a strict power-law relationship as in § 2.2, we allow the power-law slope to vary continuously with radius, described by $\tilde{\beta}(a^*)$. We define a local

approximation

$$N^*_{eq}(r) \approx \tilde{g}_{eq}(a^*) r^{\tilde{\beta}_{eq}(a^*)} \quad \text{for } r \sim a^*. \tag{3.3}$$

Applying this as well as (1.1) and (3.1) to (3.2) produces

$$h \int_{a^*}^{1} r^{\gamma+3} \, \mathrm{d}r = \tilde{g}_{eq}(a^*) \int_{a^*}^{1} r^{\tilde{\beta}_{eq}(a^*)-2/3} m \int_{0}^{a^*} r'^3 f^*(r'; r) \, \mathrm{d}r' \, \mathrm{d}r. \tag{3.4}$$

We note that for $a^{*\gamma+4} \ll 1$, the left side of (3.4) approaches the (non-dimensionalised) steady volumetric flow rate of air being injected, Q^*. As $\tilde{g}_{eq}(a^*)$ is a measure of the magnitude of $N^*_{eq}(a^*)$, and it will be shown in § 4 that $\tilde{g}_{eq}(a^* \ll 1)$ is independent of a^*, we recover the linear proportionality between $N_{eq}(a)$ and Q given by (1.2) for $a \ll a_{max}$.

To further simplify (3.4), we assume identical fragmentation (2.5). Noting that in this case the inner integral on the right side of (3.4) is only non-zero for $r < a^* m^{1/3}$, we change the upper limit of integration on the outer integral to $a^* m^{1/3}$ and obtain

$$h(\gamma+4)^{-1}[1 - a^{*\gamma+4}] = \tilde{g}_{eq}(a^*) \frac{a^{*\tilde{\beta}_{eq}(a^*)+10/3}}{\tilde{\beta}_{eq}(a^*) + 10/3} [m^{\tilde{\beta}_{eq}(a^*)/3+10/9} - 1]. \tag{3.5}$$

Applying the local equilibrium condition $\partial N_{eq}(a)/\partial t = 0$, (2.7) gives

$$a^{*-2/3}[m^{10/9} N^*_{eq}(a^* m^{1/3}) - N^*_{eq}(a^*)] + h a^{*\gamma} = 0. \tag{3.6}$$

Using the local approximation (3.3) about a^* to approximate $N^*_{eq}(a^* m^{1/3})$ gives

$$\tilde{g}_{eq}(a^*) a^{*\tilde{\beta}_{eq}(a^*)-2/3} (m^{\tilde{\beta}_{eq}(a^*)/3+10/9} - 1) + h a^{*\gamma} = 0. \tag{3.7}$$

Combining (3.5) and (3.7), we determine the relationship between $\tilde{\beta}_{eq}(a)$ and the injection power-law slope γ:

$$\tilde{\beta}_{eq}(a) = \frac{\gamma+4}{1 - (a_{max}/a)^{\gamma+4}} - 10/3. \tag{3.8}$$

We note that as $a \to a_{max}$, $\tilde{\beta}_{eq}(a)$ becomes more negative; the equilibrium slope becomes steeper for the largest bubbles. We revisit this point in § 5.

When $a_H \ll a_{max}$, most of the bubble-size distribution will follow a single power law $\beta = \tilde{\beta}_{eq}(a \ll a_{max})$. There are two distinct regimes, which are similar to those in § 2.2. The weak injection regime ($\gamma \geq -4$) has injected volume concentrated at large bubbles, and as a result the fragmentation term dominates the injection term of (2.3) at equilibrium. Here, the equilibrium slope is $\tilde{\beta}_{eq}(a \ll a_{max}) = -10/3$, independent of γ. We note that we can recover Garrett *et al.* (2000): when $\gamma = \infty$, $\tilde{\beta}_{eq}(a) = -10/3$ for all $a < a_{max}$. The strong injection regime ($\gamma < -4$) has injected volume concentrated at small bubbles, and the injection term dominates (2.3) at equilibrium. Yet fragmentation still modifies the equilibrium slope and $\tilde{\beta}_{eq}(a \ll a_{max}) = \gamma + 2/3$. In both regimes, $\tilde{\beta}_{eq}(a) \leq -10/3$, making it the upper limit of the power-law slope. We conclude by noting that in the weak regime, because $\tilde{\beta}_{eq}(a)$ is independent of γ, the equilibrium bubble-size distribution cannot be used to infer information on the underlying entrainment distribution.

Case	Daughter distribution	m	$f_V^*(V^*)$	C_f
A	S-PBM	2	$\delta(V^* - 1/2)$	1
B	Martínez-Bazán *et al.* (1999*b*)	2	$(V^*)^{2/9}(1 - V^*)^{2/9}$	1.314
C	Tsouris & Tavlarides (1994)	2	$2^{1/3} - (V^*)^{2/3} - (1 - V^*)^{2/3}$	2.255
D	Martínez-Bazán *et al.* (2010)	2	$(V^*)^{-4/9}(1 - V^*)^{-4/9}$	1.712
E	Diemer & Olson (2002)	3	$(V^*)^{1/4}(1 - V^*)^{3/2}$	1.253
F	Diemer & Olson (2002)	4	$(V^*)^{1/2}(1 - V^*)^{7/2}$	1.185

Table 1. Volume-based p.d.f.s, $f_V^*(V^*)$, of daughter distributions used in simulations and corresponding time scaling constant C_f calculated using (4.4). Note that a constant to ensure $\int f_V^*(V^*)\,\mathrm{d}V^* = 1$ is omitted for brevity.

3.2. *The influence of fragmentation daughter distribution models*

We consider here the effect of daughter distributions more realistic than the identical distribution used in § 3.1. Phenomenological daughter distributions are typically categorised as bell-shaped, U-shaped or M-shaped (Liao & Lucas 2009). We consider a binary-fragmentation ($m = 2$) daughter distribution from each category and a daughter distribution proposed by Diemer & Olson (2002) for $m \neq 2$. We assume $We = \infty$, so there is no minimum daughter-bubble radius and the daughter distributions become scale-invariant. We describe these daughter distributions using the volume-based p.d.f. $f_V^*(V^*)$ based on the relative volume $V^* = (a'/a)^3$, which is related to the radius-based p.d.f. by $af(a'; a) = 3V^{*2/3} f_V^*(V^*)$ (Martínez-Bazán *et al.* 2010). Table 1 gives the volume-based p.d.f. for each daughter distribution considered.

To confirm the validity of (3.8) for general daughter distributions, we perform two types of simulations over a broad range of γ and a_{max}/a: (a) direct numerical simulations of the S-PBM (2.7); and (*b*) Monte Carlo (MC) simulations where fragmentation following (1.1) and injection following SIM are modelled as Poisson processes over each fixed Δt. Direct simulation of (2.7) is inexpensive because it is deterministic, but it is applicable only for identical daughter distributions (case A in table 1 for $m = 2$). In these simulations, discretisation of radius is done on a logarithmic scale and Heun's method is used for time marching. MC simulations are computationally more expensive, but capture the stochastic nature of fragmentation and entrainment and are applicable for general daughter distributions. MC simulations are performed for cases in table 1 where the daughter bubbles from each fragmentation event are chosen using random sampling of the respective distributions. Due to the power-law nature of bubble-size distributions, the simulated distributions are averaged over logarithmic intervals based on $m^{1/3}$:

$$\langle N(a)\rangle_m = (a(m^{1/3} - 1))^{-1} \int_a^{a\,m^{1/3}} N(a')\,\mathrm{d}a', \tag{3.9a}$$

$$\langle \tilde{\beta}(a)\rangle_m = 3\ln(\langle N(a)\rangle_m / \langle N(a\,m^{-1/3})\rangle_m)/\ln(m). \tag{3.9b}$$

We establish convergence for both simulation types with $\Omega(a)\Delta t = 1/100$ and 30 bins per $m^{1/3}$ interval for the radius discretisation of S-PBM. The results of the S-PBM and MC simulations are compared to (3.8) in figure 1 and show good agreement. These simulations demonstrate that the equilibrium slope predicted by (3.8), although based on the simplifying assumption of identical fragmentation, is, in fact, applicable to general daughter distributions. This is consistent with the observation by Qi *et al.* (2020) that

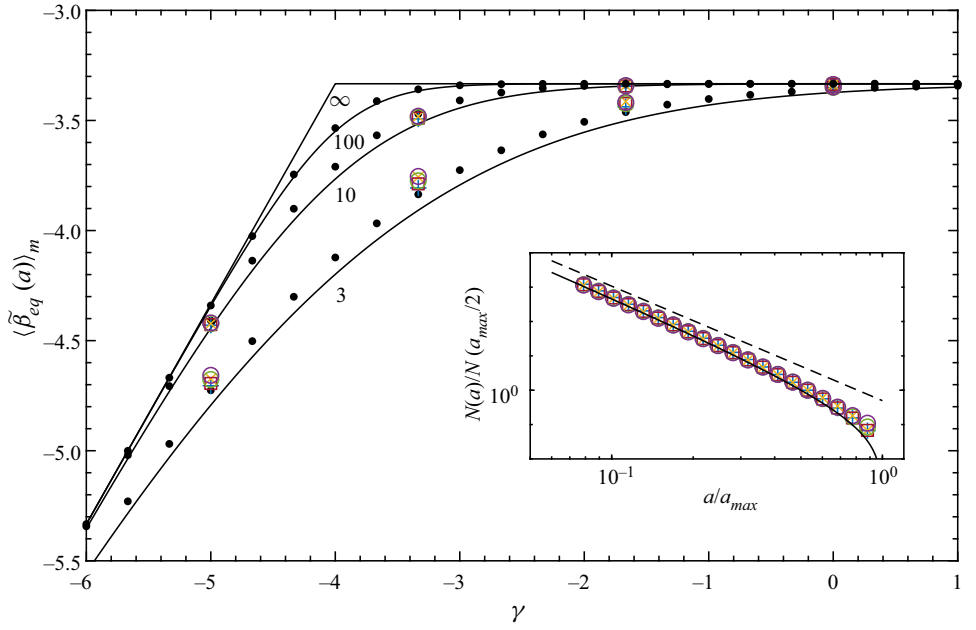

Figure 1. Comparison of equilibrium local power-law slopes resulting from SIM with a range of injection power-law slopes γ, as modelled by (3.8) (——); case A (•); case B (+, blue); case C (×, yellow); case D (□, red); case E (○, green); case F (○, purple). Case A is calculated using direct numerical simulations, cases B–F using MC simulations. The value of a_{max}/a for the reported $\langle \tilde{\beta}_{eq}(a) \rangle_m$ is indicated below each data set. For the MC simulations, the inset shows the equilibrium bubble-size distributions for $\gamma = -10/3$ compared to $\propto a^{-10/3}$ (- - - -).

the choice of daughter distribution has no effect on the equilibrium power-law slope for fragmentation cascades.

4. Time scale of convergence to the equilibrium distribution

We investigate the convergence time τ such that $N(a, t > t_0 + \tau) \approx N_{eq}(a)$, where $N(a, t_0) = 0$. First, we revisit the global equilibrium condition (3.4). Rewriting it in terms of f_V^*, we have

$$h \int_{a^*}^{1} r^{\gamma+3} \, \mathrm{d}r = \tilde{g}_{eq}(a^*) \frac{m}{3} a^{*\tilde{\beta}_{eq}(a^*)+10/3} \int_{a^{*3}}^{1} u^{-\tilde{\beta}_{eq}(a^*)/3-19/9} \int_0^u v f_V^*(v) \, \mathrm{d}v \, \mathrm{d}u. \quad (4.1)$$

For weak injection, we consider the limiting case $a^* \to 0$. By (3.8), $\tilde{\beta}_{eq}(a^*) = -10/3$ and we can simplify (4.1):

$$\frac{h}{\gamma + 4} = \tilde{g}_{eq}(a^* \ll 1) \frac{m}{3} \int_0^1 u^{-1} \int_0^u v f_V^*(v) \, \mathrm{d}v \, \mathrm{d}u. \quad (4.2)$$

Rearranging (4.2), we define a new constant C_f to quantify the effect of f_V^* on $\tilde{g}_{eq}$ and scale C_f so that for an identical daughter distribution, (2.5), it has a value of unity:

$$\tilde{g}_{eq}(a^* \ll 1) = \frac{3}{\ln(m)} \frac{h}{\gamma + 4} C_f; \quad C_f = \frac{\ln(m)/m}{\displaystyle\int_0^1 \int_0^1 uw f_V^*(uw) \, \mathrm{d}w \, \mathrm{d}u}. \quad (4.3a,b)$$

Table 1 shows the numerically calculated values of C_f.

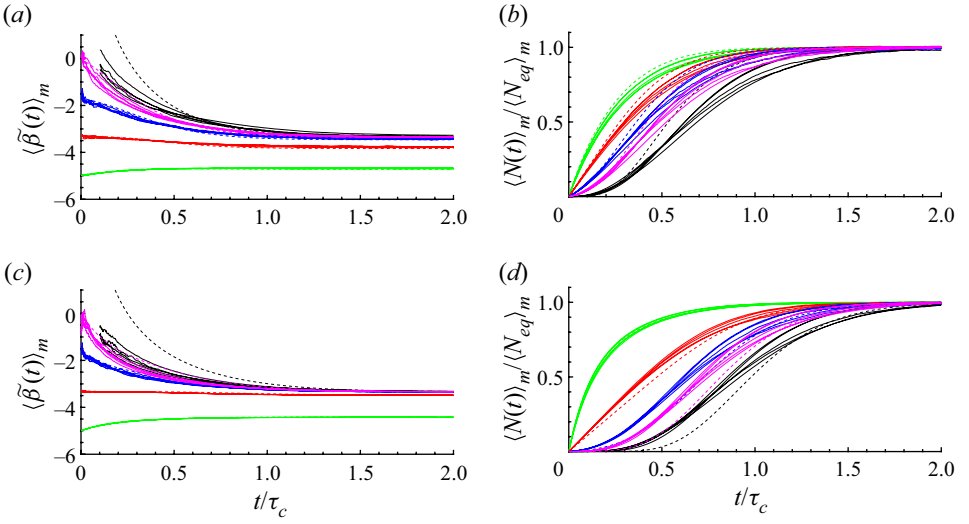

Figure 2. Evolution of bubble-size distribution N (b and d) and local power-law slope $\tilde{\beta}$ (a and c) as measured at $a_{max}/a = 3$ (a and b) and $a_{max}/a = 10$ (c and d). Numerical simulations of case A (- - - -) and MC simulations (———) of cases B–F (cf. table 1). Colours based on γ: green, $\gamma = -5$; red, $\gamma = -10/3$; blue, $\gamma = -5/3$; magenta, $\gamma = 0$; black, $\gamma = \infty$ (single-radius injection). Note that $\tilde{\beta}(t \ll \tau_c)$ is not reported for MC simulations of $\gamma = \infty$ due to significant noise.

We write the varying power-law slope description of the bubble-size distribution N_{eq} from § 3.1, now as a function of time: $N^*(a^*, t^*) \approx \tilde{g}(a^*, t^*)a^{*\tilde{\beta}(a^*,t^*)}$. With the dependence on a^* omitted for clarity, $\tilde{g}(t)$ has a Taylor approximation to first order: $\hat{g}(t) = \tilde{g}(t_0) + (t - t_0)\tilde{g}'(t_0)$. Using (2.3) and $\tilde{g}(t_0) = 0$, we obtain $\tilde{g}'(t_0) = ha^{*\gamma-\tilde{\beta}(a^*,t_0)}$. Note that we neglected the time dependence of $\tilde{\beta}(a^*, t)$ (cf. figure 2), making $\hat{g}(t)$ a poor description of the general evolution of $N^*(a^*, t^*)$. However for the special case $\gamma = -10/3$ and $a^* \ll 1$, $\tilde{\beta}(a^*, t) = \gamma$ and we can define a critical time τ_c such that $\hat{g}(t_0 + \tau_c) = \tilde{g}_{eq}(a^* \ll 1)$:

$$\tau_c = (9/2)(\ln m)^{-1}(C_f/C_\Omega)\varepsilon^{-1/3}a_{max}{}^{2/3}. \tag{4.4}$$

Despite the special case used in deriving (4.4), numerical simulations of S-PBM and MC simulations of realistic daughter distributions (cf. § 3.2) show that τ_c provides a general time scaling, with equilibrium reached at $\tau \approx 2\tau_c$ for weak injection and $\tau \lesssim \tau_c$ for strong injection. Figure 2 shows results from simulations of $a_{max}/a = 3$ and $a_{max}/a = 10$. The S-PBM simulations of larger a_{max}/a (not shown) demonstrate similar behaviour for weak injection, with τ/τ_c becoming smaller for strong injection. Figure 2 provides a direct means to validate (4.4) experimentally if the relevant underlying parameters are known or can be measured; and an indirect means to deduce the shape of the daughter distribution if the evolution of the bubble-size distributions can be quantitatively obtained.

We make two comments on (4.4). First, although we consider power-law injection rather than single-radius injection, the dependence of τ_c on m (disregarding C_f) is similar to the equation (1.3) proposed by Deike *et al.* (2016). For $We = \infty$ and small m, $c_{\infty,m} = 1 - 1/(m^{-1/3} - 1) \sim (9/2)(\ln m)^{-1}$. Considering a more typical $a_H/a_{max} \approx 10$, for binary breakup ($m = 2$) the coefficient for τ_c in (4.4) is $(9/2)(\ln 2)^{-1} \approx 6.5$, and for tertiary breakup ($m = 3$) the coefficient is $(9/2)(\ln 3)^{-1} \approx 4.1$. These values compare

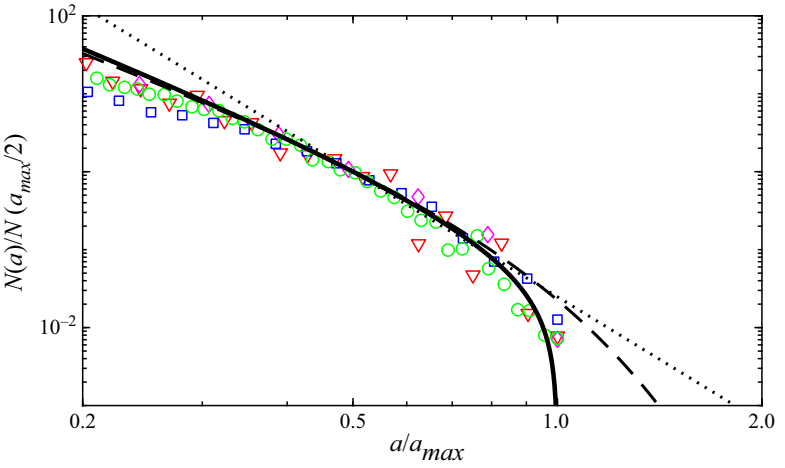

Figure 3. Comparison of N_{eq} prediction from (3.8) ($\gamma = -10/3$) (——-) with existing theories: - - -, equation (3.7) of Deike *et al.* (2016); · · · · · ·, $\propto a^{-16/3}$ (Garrett *et al.* 2000). Experiments: (i) □ (blue), figure 5 of Deane *et al.* (2016), case A. Simulations: (ii) ▽ (red), figure 7(*e*) of Deike *et al.* (2016); (iii) ◇ (magenta), figure 8 of Hendrickson *et al.* (2020), $Fr = 0.192$; (iv) ○ (green), figure 4d of Chan *et al.* (2021). Values for a_H/a_{max} are approximately 0.35, 0.15, 0, 0.15 respectively for (i), (ii), (iii), (iv).

well with those obtained from the simulations of Deike *et al.* (2016). Second, the value of C_f provides a new quantification of the dependence of τ_c on f_V^* first described by Qi *et al.* (2020): the closer a daughter distribution is to identical fragmentation, the faster the convergence to equilibrium. Through C_f, observed convergence times now provide a mechanism to evaluate daughter distributions.

We compare τ_c to the time scale of entrainment by breaking waves. In laboratory experiments by Deane & Stokes (2002), $\varepsilon \approx 13\text{W kg}^{-1}$ and $a_{max} \approx 10$ mm. The reported time period for entrainment was $T_E \approx 1$ s. For illustration, using $C_f = 1.5$ and $m = 2$ yields $\tau_c \approx 0.5$ s, and thus $T_E/\tau_c \approx 2$. This suggests the bulk bubble-size distribution observed by Deane & Stokes (2002) at the end of T_E would have approached N_{eq}. The fast convergence of N and $\tilde{\beta}$ demonstrates that fragmentation quickly obscures the effect of entrainment. In fact, although initially $\tilde{\beta}(a, 0) = \gamma$, $\tilde{\beta}(a, t)$ approaches $\tilde{\beta}_{eq}(a)$ approximately exponentially. Thus, even for $t \ll \tau_c$, $\tilde{\beta}(a, t)$ does not give a reliable measure of γ. Therefore, the commonly observed $\beta \approx -10/3$ for $a > a_H$ should only be considered evidence of $\gamma \geq -4$, not of $\gamma = -10/3$ (Yu *et al.* 2020). As neither $\tilde{\beta}_{eq}(a)$ (cf. § 3) nor $\tilde{\beta}(a, t)$ provides reliable insight into γ for weak injection, further investigation of $I(a)$ will likely require new experimental and computational techniques near the free surface to allow direct identification and measurement of entraining bubbles.

5. Steepening of size distribution due to fragmentation and entrainment

It has been previously noted (Deike *et al.* 2016) that bubble-size distributions deviate from a power law and become steeper for a around a_{max}. Figure 3 shows bubble-size distributions from experiments and computational fluid dynamics simulations (scaled by a_{max}) of different entraining flows that exhibit such steepening. The distributions generally agree for $a \lesssim a_{max}$, but are not expected to be good for a near a_H (different values of a_H/a_{max} for the data are listed in the figure caption). As large bubbles rise faster (Thorpe 1982), the steepening for a around a_{max} has generally been attributed to degassing (Deike

et al. 2016; Chan *et al.* 2021). Garrett *et al.* (2000) and Deike *et al.* (2016) provided models for steepening due to degassing, also shown in figure 3.

Because of the fast convergence discussed in § 4, we expect to observe $\tilde{\beta}_{eq}(a)$ given by (3.8) during active entrainment. In figure 3, we include $\tilde{\beta}_{eq}(a)$ using $\gamma = -10/3$ (Yu *et al.* 2020). Note that the shape does not change significantly with moderate variation of γ. From figure 3, we see that (3.8) exhibits the steepening of the bubble-size distribution for $a \sim a_{max}$, somewhat corroborated by existing measurements and simulations. Since (3.8) accounts only for fragmentation and cutoff power-law entrainment, this reveals a new mechanism for steepening deviation from a power law independent of other mechanisms such as degassing. The relative importance of these different mechanisms is a subject of current research.

6. Conclusion

We have developed a population balance model for a fragmentation cascade driven by steady injection $I(a)$, described by power-law slope γ and large-radius cutoff a_{max}. Where previous work has either considered fragmentation (Garrett *et al.* 2000) or power-law entrainment (Yu *et al.* 2020), this approach allows us to study the interaction between the two and its effect on the equilibrium and evolution of bulk bubble-size distributions for large bubbles in air-entraining bubbly flow.

We first seek the equilibrium bulk bubble-size distribution $N_{eq}(a)$. We describe its shape using a local power-law slope $\tilde{\beta}_{eq}(a)$, which we find is dependent on a_{max} and γ. As previously observed (Qi *et al.* 2020), $\tilde{\beta}_{eq}(a)$ does not depend on the choice of fragmentation daughter distribution. We identify two regimes of injection: weak injection for $\gamma \geq -4$, with $\tilde{\beta}_{eq}(a \ll a_{max}) = -10/3$, and strong injection for $\gamma < -4$, with $\tilde{\beta}_{eq}(a \ll a_{max}) = \gamma + 2/3$. For weak injection, $\tilde{\beta}_{eq} = -10/3$ agrees with power-law slope $\beta = -10/3$ commonly observed for $a > a_H$, providing a generalized explanation which builds on that proposed by Garrett *et al.* (2000). The independence of $\tilde{\beta}_{eq}$ on γ in the weak regime suggests that the observed (equilibrium) slope $\beta = -10/3$ may result from different underlying (weak) entrainment mechanisms.

We show that the time scale to reach the equilibrium distribution $N_{eq}(a)$ (after initiation of entrainment) is given by $\tau_c \propto C_f\, \varepsilon^{-1/3} {a_{max}}^{2/3}$, where C_f is a constant expressing the effect of the fragmentation daughter distribution. The latter can thus be elucidated by quantifying τ_c (using figure 2, for example). For small τ_c, the bulk bubble-size distribution rapidly evolves away from the initial distribution $N(a, 0) \propto I(a)$; thus the mechanism of the entrainment itself might not be accessible from bulk measurements. Finally, we show that the reported steepening deviation of $N_{eq}(a)$ from a power law for a around a_{max} happens due to interaction between entrainment and fragmentation alone, even in the absence of mechanisms such as degassing.

Funding. This work was funded by the U.S. Office of Naval Research grant N00014-20-1-2059 under the guidance of Dr W.-M. Lin. The computational resources were funded through the Department of Defense High Performance Computing Modernization Program.

Declaration of interest. The authors report no conflict of interest.

Author ORCIDs.
Declan B. Gaylo https://orcid.org/0000-0001-6198-7003;
Kelli Hendrickson https://orcid.org/0000-0002-3596-6556;
Dick K.P. Yue https://orcid.org/0000-0003-1273-9964.

References

Blenkinsopp, C.E. & Chaplin, J.R. 2010 Bubble size measurements in breaking waves using optical fiber phase detection probes. *IEEE J. Ocean. Engng* **35**, 388–401.

Castro, A.M., Li, J. & Carrica, P.M. 2016 A mechanistic model of bubble entrainment in turbulent free surface flows. *Intl J. Multiphase Flow* **86**, 35–55.

Chan, W.H.R., Johnson, P.L., Moin, P. & Urzay, J. 2021 The turbulent bubble break-up cascade. Part 2. Numerical simulations of breaking waves. *J. Fluid Mech.* **912**, A43.

Deane, G.B. & Stokes, M.D. 2002 Scale dependence of bubble creation mechanisms in breaking waves. *Nature* **418**, 839–844.

Deane, G.B., Stokes, M.D. & Callaghan, A.H. 2016 The saturation of fluid turbulence in breaking laboratory waves and implications for whitecaps. *J. Phys. Oceanogr.* **46**, 975–992.

Deike, L., Melville, W.K. & Popinet, S. 2016 Air entrainment and bubble statistics in breaking waves. *J. Fluid Mech.* **801**, 91–129.

Diemer, R.B. & Olson, J.H. 2002 A moment methodology for coagulation and breakage problems: Part 3 – generalized daughter distribution functions. *Chem. Engng Sci.* **57**, 4187–4198.

Garrett, C., Li, M. & Farmer, D. 2000 The connection between bubble size spectra and energy dissipation rates in the upper ocean. *J. Phys. Oceanogr.* **30** (9), 2163–2171.

Hendrickson, K., Yu, X. & Yue, D.K.P. 2020 Towards development of air entrainment models for ship wakes. In *Proceedings of the 33rd Symposium on Naval Hydrodynamics*. U.S. Office of Naval Research and The Osaka University.

Hinze, J.O. 1955 Fundamentals of the hydrodynamic mechanism of splitting in dispersion processes. *AIChE J.* **1**, 289–295.

Lewis, D.A. & Davidson, J.F. 1982 Bubble splitting in shear flow. *Trans. Inst. Chem. Engrs* **60**, 283–291.

Liao, Y. & Lucas, D. 2009 A literature review of theoretical models for drop and bubble breakup in turbulent dispersions. *Chem. Engng Sci.* **64**, 3389–3406.

Martínez-Bazán, C., Montañés, J.L. & Lasheras, J.C. 1999*a* On the breakup of an air bubble injected into a fully developed turbulent flow. Part 1. Breakup frequency. *J. Fluid Mech.* **401**, 157–182.

Martínez-Bazán, C., Montañés, J.L. & Lasheras, J.C. 1999*b* On the breakup of an air bubble injected into a fully developed turbulent flow. Part 2. Size pdf of the resulting daughter bubbles. *J. Fluid Mech.* **401**, 183–207.

Martínez-Bazán, C., Rodríguez-Rodríguez, J., Deane, G.B., Montaes, J.L. & Lasheras, J.C. 2010 Considerations on bubble fragmentation models. *J. Fluid Mech.* **661**, 159–177.

Mukherjee, S., Safdari, A., Shardt, O., Kenjereš, S.Ša & Van den Akker, H.E.A. 2019 Droplet–turbulence interactions and quasi-equilibrium dynamics in turbulent emulsions. *J. Fluid Mech.* **878**, 221–276.

Patwardhan, A.W., Mali, R.G., Jadhao, S.B., Bhor, K.D., Padmakumar, G. & Vaidyanathan, G. 2012 Argon entrainment into liquid sodium in fast breeder reactor. *Nucl. Engng Des.* **249**, 204–211.

Qi, Y., Mohammad Masuk, A.U. & Ni, R. 2020 Towards a model of bubble breakup in turbulence through experimental constraints. *Intl J. Multiphase Flow* **132**, 103397.

Rodríguez-Rodríguez, J., Gordillo, J.M. & Martínez-Bazán, C. 2006 Breakup time and morphology of drops and bubbles in a high-reynolds-number flow. *J. Fluid Mech.* **548**, 69–86.

Skartlien, R., Sollum, E. & Schumann, H. 2013 Droplet size distributions in turbulent emulsions: breakup criteria and surfactant effects from direct numerical simulations. *J. Chem. Phys.* **139**, 174901.

Thorpe, S.A. 1982 On the clouds of bubbles formed by breaking wind-waves in deep water, and their role in air-sea gas transfer. *Phil. Trans. R. Soc. Lond.* A **304**, 155–210.

Tsouris, C. & Tavlarides, L.L. 1994 Breakage and coalescence models for drops in turbulent dispersions. *AIChE J.* **40**, 395–406.

Valentas, K.J., Bilous, O. & Amundson, N.R. 1966 Analysis of breakage in dispersed phase systems. *Ind. Engng Chem. Fundam.* **5**, 271–279.

Wang, Z., Yang, J. & Stern, F. 2016 High-fidelity simulations of bubble, droplet and spray formation in breaking waves. *J. Fluid Mech.* **792**, 307–327.

Williams, F.A. 1985 *Combustion Theory*, 2nd edn. Benjamin/Cummings.

Yu, X., Hendrickson, K., Campbell, B.K. & Yue, D.K.P. 2019 Numerical investigation of shear-flow free-surface turbulence and air entrainment at large Froude and Weber numbers. *J. Fluid Mech.* **880**, 209–238.

Yu, X., Hendrickson, K. & Yue, D.K.P. 2020 Scale separation and dependence of entrainment bubble-size distribution in free-surface turbulence. *J. Fluid Mech.* **885**, R2.